Branching behavior of standing waves—The signatures of resonance

D. H. Smith and A. J. Roberts
Department of Mathematics and Computing, University of Southern Queensland, Toowoomba QLD 4350, Australia

Arclength continuation methods are used to conduct a detailed branching study of standing wave solutions for fluids in a rectangular container, using depth and crest acceleration as control parameters. At each depth the applicable acceleration range extends between zero and one, and a number of multiple solution structures are uncovered. An intimate connection is established between these structures and the phenomenon of harmonic resonance. © *1999 American Institute of Physics.* [S1070-6631(99)02305-3]

I. INTRODUCTION

Resonance is a phenomenon coinciding with zero divisors in perturbation solution coefficients, and can be interpreted as a critical response of the linear part of a system to the forcing terms from the nonlinear part. In the context of water waves, resonance is associated with a specific energy sharing mechanism between certain interacting wave components,[1] causing the growth of some modes at the expense of others. A key manifestation of resonance is the occurrence of multiple solutions and associated bifurcation behavior, which is the main focus of this paper for the case of standing gravity waves.

Water wave resonance behavior has received considerable attention in a variety of flow configurations. For finite depth capillary–gravity waves resonance is associated with critical wave numbers at which a normal perturbation solution breaks down.[2] The critical wave numbers are depth dependent and multiple solutions are possible at or near these resonant values. In a numerical study of steady gravity–capillary waves on infinitely deep water, Chen and Saffman[3] linked nonuniqueness to a resonance mechanism, and produced corresponding bifurcation diagrams illustrating multiple solution behavior. Toland and Jones[4] reinforced this work via an integral equation formulation, demonstrating an array of possible primary and secondary bifurcation behavior. More recently, Okamoto and Shoji[5] used a Levi-Civita capillary–gravity wave formulation with spectral collocation to study resonance and bifurcation behavior associated with specific wave mode interactions. Nonphysical *self-intersecting* waves were included in the computed solutions, providing essential branch links between physical portions. Related work by Aston[6] computed actual *paths* of bifurcation points originating from mode interaction points, confirming a substantial increase in complexity as surface tension is reduced, or gravity becomes dominant. Pure gravity waves, which cannot be obtained as the continuous limit of capillary–gravity waves for vanishing surface tension, were considered by Chen and Saffman[7] using an integrodifferential equation formulation. Nonuniqueness behavior was also observed for sufficiently large waveheights.

Previous studies of standing finite-depth gravity waves offer little insight into the realms of multiple solution behavior. Vanden-Broeck and Schwartz[8] used a series truncation method, expanding the surface elevation and velocity potential, to produce frequency–steepness curves for small-amplitude waves. Their computed results indicated the existence of two different standing waves with the same frequency at certain depths, but the matter was not pursued beyond this stage. Tadjbakhsh and Keller[9] provided a uniqueness condition for standing waves, defining critical depths at which the linear frequency of some harmonic is an integral multiple of the fundamental frequency. In a subsequent perturbation solution to third order, nonuniqueness was not explored. Considerably more light was thrown onto the phenomenon by Concus,[10] who considered standing capillary–gravity waves. Concus gave a modified uniqueness condition, defining critical depths that were shown to generate zero denominators in the perturbation solution coefficients, or resonance. Near these resonant depths it was emphasized that small nonzero denominators would produce very large solution contributions from particular harmonics, a fact with crucial implications on the validity of the perturbation solutions. While not specifically addressing such implications, Vanden-Broeck[11] was able to construct a perturbation solution valid at the first critical depth, clearly demonstrating multiple solutions. Comparisons with computed results at neighboring depths using the scheme in Ref. 8 identified Vanden-Broeck's two solutions as members of distinct solution families.

In a later study,[12] Concus examined the uniqueness condition without surface tension and showed that the corresponding excluded depths formed a denumerably infinite set that is densely distributed on $(0, \infty)$. At any depth there are infinitely many resonant or near resonant terms in a full perturbation expansion, which means that high-order terms of comparable magnitude to the low-order terms will be lost in the truncation. Modifications to the perturbation solution must be made to account for this.

In this numerical study a suitable continuation procedure is coupled to a semi-Lagrangian boundary integral/Runge–Kutta discretization of the hydrodynamic equations to permit a comprehensive exploration of the depth-crest acceleration,

     1051

(d, A_c), parameter space. At any depth, solutions to the resulting nonlinear system of equations are continued in A_c using pseudoarclength continuation,[13] a process developed specifically to handle singular branch points. For branching diagram purposes, computed frequency is chosen as the representative standing wave property, and this is plotted against A_c for a range of depths. Detailed diagrams are generated, uncovering a richness of bifurcation behavior that clearly signifies harmonic resonance. Resonant depths, as predicted from the uniqueness conditions described earlier, are found to occupy upper bounds of depth ranges in which the resonant activity persists in the branching diagrams.

II. CALCULATION OF FINITE DEPTH STANDING WAVES

A. Governing equations and boundary integral formulation

The inviscid, incompressible, potential flow is bounded above by a free surface, laterally by parallel vertical walls and below by a horizontal solid surface. Laplace's equation holds in the fluid for the velocity potential ϕ,

$$\nabla^2 \phi(x,y,t) = 0, \tag{1}$$

while kinematic and dynamic conditions,

$$\phi_y = \eta_t + \phi_x \eta_x, \tag{2}$$

$$\phi_t = -\tfrac{1}{2}q^2 - g\,\eta, \tag{3}$$

where q is the fluid velocity magnitude and g is the acceleration due to gravity, apply on the free surface $y = \eta(x,t)$. Lengths and times are made dimensionless with respect to $L/2\pi$ and $\sqrt{L/(2\pi g)}$, respectively, where L is the wavelength. Solid boundary conditions,

$$\phi_x = 0, \tag{4}$$

apply on the vertical walls at $x = 0$ and π while

$$\phi_y = 0, \tag{5}$$

holds on the horizontal lower boundary $y = -d$. Finally, the zero mean height condition,

$$\bar{\eta}(t) = \int_0^{2\pi} \eta(x,t)\,dx = 0, \tag{6}$$

is also imposed, serving as an additional mass conservation measure.

The free surface can be represented as an infinite, periodic vortex sheet separating two fluids,[14] with the upper fluid of zero density. Imposing symmetry about $x = 0$ gives motion between two vertical walls separated by half a wavelength, and reflecting the sheet about $y = -d$ satisfies the horizontal boundary condition, giving the complex potential

$$f(z,t) = \phi(x,y,t) + i\psi(x,y,t)$$

$$= -\frac{i}{2\pi} \int_{-\infty}^{\infty} a(j,t)\{\log[z - Z(j,t)]$$

$$- \log[z - \bar{Z}(j,t) + 2id]\}dj,$$

where $a(j,t)$ is the vortex strength per unit parameter j, t is time, and z is a field point off the free surface. $Z(j,t)$ is a material point on the free surface and overbars denote the complex conjugate. Imposing periodicity, with spatial period N and differentiating gives the complex velocity field

$$\bar{q}(z,t) = u - iv$$

$$= -\frac{i}{4\pi} \int_0^N a(j,t)$$

$$\times \left[\cot\left(\frac{z - Z(j,t)}{2}\right) - \cot\left(\frac{z - \bar{Z}(j,t) + 2id}{2}\right) \right] dj, \tag{7}$$

where u and v are the horizontal and vertical velocity components. Moving z onto the free surface then gives the singular integral equation

$$\frac{\partial \phi(k,t)}{\partial j} = \frac{1}{2} a(k,t) + \frac{1}{4\pi} \int_0^N a(j,t)\,\Im$$

$$\left\{ \frac{\partial Z(k,t)}{\partial j} \left[\cot\left(\frac{Z(k,t) - Z(j,t)}{2}\right) \right.\right.$$

$$\left.\left. - \cot\left(\frac{Z(k,t) - \bar{Z}(j,t) + 2id}{2}\right) \right] \right\} dj,$$

for the vortex strength $a(k,t)$ at surface point $Z(k,t)$. After solving this the free surface velocities $[U(k,t), V(k,t)]$ can be calculated from (7) and material surface points $Z(k,t) = X(k,t) + iY(k,t)$ then move according to

$$\frac{\partial X(k,t)}{\partial t} = U(k,t), \tag{8}$$

$$\frac{\partial Y(k,t)}{\partial t} = V(k,t), \tag{9}$$

while the corresponding velocity potential evolves according to

$$\frac{\partial \phi(k,t)}{\partial t} = -Y(k,t) + \frac{1}{2}[U^2(k,t) + V^2(k,t)]. \tag{10}$$

B. Discretization and numerical solution

After choosing a spatial discretization N, the discrete integral equation to be solved for the vortex strengths a_k becomes

$$\phi'_k = \left[\frac{1}{2} + \frac{1}{4\pi} \Im\left(\frac{Z''_k}{Z'_k} \right) \right] a_k + \frac{1}{4\pi}$$

$$\times \sum_{j=0, j\neq k}^{N/2} a_j \Im\left[Z'_k \cot\left(\frac{Z_k - Z_j}{2} \right) \right]$$

$$- \frac{1}{4\pi} \sum_{j=1}^{N/2-1} a_j \Im\left\{ Z'_k \left[\cot\left(\frac{Z_k + \bar{Z}_j}{2} \right) \right. \right.$$

$$\left. \left. - \cot\left(\frac{Z_k + Z_j + 2id}{2} \right) \right] \right\}$$

$$- \frac{1}{4\pi} \sum_{j=0}^{N/2} a_j \Im\left[Z'_k \cot\left(\frac{Z_k - \bar{Z}_j + 2id}{2} \right) \right], \tag{11}$$

for $k=0,...,N/2$, which is a diagonally dominant linear system of equations. Primes refer to differentiation with respect to the surface parameter j, which is implemented spectrally. The discrete surface velocity is then given by the summation

$$\bar{q}_k = \frac{a_k}{2Z'_k} - \frac{i}{4\pi} \left(\frac{Z''_k a_k}{(Z'_k)^2} - \frac{2a'_k}{Z'_k} \right)$$

$$- \frac{i}{4\pi} \sum_{j=0, j\neq k}^{N/2} a_j \cot\left(\frac{Z_k - Z_j}{2} \right)$$

$$+ \frac{i}{4\pi} \sum_{j=1}^{N/2-1} a_j \left[\cot\left(\frac{Z_k + \bar{Z}_j}{2} \right) - \cot\left(\frac{Z_k + Z_j + 2id}{2} \right) \right]$$

$$+ \frac{i}{4\pi} \sum_{j=0}^{N/2} a_j \cot\left(\frac{Z_k - \bar{Z}_j + 2id}{2} \right), \quad k=0,...,N/2, \tag{12}$$

which is a trapezium evaluation of (7) with appropriate singularity treatment.[14] Substitution of the discrete velocities in (8), (9), and (10) then completes the semidiscrete equation system. This is a two-parameter, implicit nonlinear system of ODEs,

$$\frac{d\mathbf{u}}{dt} = \mathbf{f}(\mathbf{u}, A_c, d), \tag{13}$$

where $\mathbf{u}$ contains the discrete surface coordinates and potentials (X_j, Y_j, ϕ_j), and A_c is the initial downward acceleration at the left wall,

$$A_c = \frac{\partial V(0,0)}{\partial t},$$

an identifying parameter closely related to wave steepness. All time integration is carried out with an explicit fourth-order Runge–Kutta scheme.

C. Standing wave solutions, continuation in parameters

Standing waves are time-periodic solutions of the semidiscrete equations, satisfying the boundary value problem,

$$\frac{d\mathbf{u}}{dt} = \mathbf{f}(\mathbf{u}, A_c, d), \quad 0 < t < T$$

$$\mathbf{u}(0) = \mathbf{u}(T),$$

where T is the unknown period. By integrating the ODE system in time through one period or part thereof and then applying appropriate periodicity conditions the boundary value problem is recast as a system of nonlinear equations. Shooting methods seek solutions of this nonlinear system by iterative procedures and will be used throughout.

The actual solutions being sought here represent initial ($t=0$) wave profiles with zero velocity that repeat themselves one period later, for given parameters A_c and d. Taking surface velocity potentials $\phi_k(0)=0$ and using spatial symmetry with N surface points per wavelength leaves $N+2$ unknowns to be found,

$$\mathbf{v} = [X_1(0),...,X_{N/2-1}(0), Y_0(0),...,Y_{N/2}(0), T, \alpha],$$

where α is the surface deviation from antisymmetry in ϕ at the quarter-period. This is an extra variable specially introduced to facilitate enforcement of the zero mean height condition (6) at $t=0$, which is numerically evaluated with the trapezium rule,

$$\bar{\eta}(0) \approx \sum_{k=1}^{N} Y(k,0) \frac{\partial X}{\partial j}(k,0) = 0.$$

A second equation comes from enforcing the prescribed crest acceleration via differencing in time,

$$A_c = \frac{V(0,\Delta t) - V(0,0)}{\Delta t},$$

while the remaining N equations are defined by integrating in time through a quarter-period and imposing the conditions

$$X_j(T/4) = \frac{2\pi}{N} j + B \sin\frac{4\pi}{N} j, \quad j=1,...,N/2-1,$$

$$Y_j(T/4) = Y_{N/2+2-j}(T/4), \quad j=0,...,N/4-1$$

$$\phi_j(T/4) = -\phi_{N/2+2-j}(T/4) + \alpha, \quad j=0,...,N/4.$$

Use of the extra variable α in the last line essentially amounts to adding a time-dependent function to the velocity potential ϕ, which has no effect on the flow dynamics. The parameter B controls the surface X coordinate spacing at $T/4$, providing minor grid adjustments when needed for extreme waves with A_c close to 1.

Assembling the equations produces a parametrized nonlinear system,

$$\mathbf{g}(\mathbf{v}, A_c, d) = \mathbf{0},$$

to be solved across the physical range of crest accelerations, $0 < A_c < 1$, for various depths. This demands a nonlinear sys-

tem solver in conjunction with a continuation procedure to cover the A_c range at each depth. Pseudoarclength continuation[13] is extremely effective for this purpose, being readily capable of handling the various singular points likely to be encountered, for example, turning points and bifurcation points. To briefly describe the technique, hold d constant and consider a parametrization of the solution $[\mathbf{v}(s), A_c(s)]$, where s is the arclength along the solution curve, implicitly defined by normalizing the tangent vector,

$$\|\dot{\mathbf{w}}\|^2 = \|\dot{\mathbf{v}}(s)\|^2 + |\dot{A}_c(s)|^2 = 1.$$

Given a solution point $\mathbf{w}_j = [\mathbf{v}(s_j), A_c(s_j)]^T$ at $s = s_j$ the new solution $\mathbf{w}_{j+1}$ at $s_{j+1} = s_j + \Delta s$ satisfies the augmented system,

$$\mathbf{G}(\mathbf{w}_{j+1}) = \begin{bmatrix} \mathbf{g}(\mathbf{w}_{j+1}) \\ (\mathbf{w}_{j+1} - \mathbf{w}_j)^T \dot{\mathbf{w}}_j - \Delta s \end{bmatrix} = \mathbf{0}, \tag{14}$$

which says that $\mathbf{w}_{j+1}$ lies on a hyperplane distant Δs from $\mathbf{w}_j$ and normal to the tangent vector $\dot{\mathbf{w}}_j$, hence the ''pseudoarclength'' property. Tangent vectors $\dot{\mathbf{w}}_j = [\dot{\mathbf{v}}(s_j), \dot{A}_c(s_j)]^T$ can be approximated by secants,

$$\dot{\mathbf{w}}_j \approx \frac{\mathbf{w}_j - \mathbf{w}_{j-1}}{\Delta s},$$

except at the first step, when a previous solution $\mathbf{w}_{j-1}$ is unavailable. In this case the linear system,

$$\frac{\partial \mathbf{g}}{\partial \mathbf{v}} \frac{\dot{\mathbf{v}}}{\dot{A}_c} = -\frac{\partial \mathbf{g}}{\partial A_c},$$

obtained by differentiating $\mathbf{g}[\mathbf{v}(s), A_c(s)] = \mathbf{0}$ with respect to s, is solved for $\dot{\mathbf{v}}/\dot{A}_c$, from which a normalized tangent is easily constructed. To switch solution branches simply requires a sufficiently large increment Δs in (14), which is solved with Newton-type methods.

D. Integral invariants

As a final check on the computed results, integral invariants for the motion can be calculated as the wave evolves through one period. The invariants are expressed in terms of quantities on the free surface[14] and include total energy,

$$\frac{1}{4\pi} \int_0^N \{\phi(j,t)[X'(j,t)V(j,t) - Y'(j,t)U(j,t)] $$
$$ + Y^2(j,t)X'(j,t)\} dj,$$

the average volume flux across the surface, which is zero,

$$\frac{1}{2\pi} \int_0^N [V(j,t)X'(j,t) - U(j,t)Y'(j,t)] dj = 0,$$

mean surface elevation,

$$\frac{1}{2\pi} \int_0^N Y(j,t)X'(j,t) dj = 0,$$

which is also zero, and the difference between the horizontal average momentum component and the momentum of the undisturbed shear flow,

$$\frac{1}{2\pi} \int_0^N Y(j,t)\phi'(j,t) dj.$$

If variations in any of these quantities become too large during one period, then a spatial grid refinement, N, will be required.

III. NUMERICAL RESULTS

A. Frequency curves and branching behavior

The computed results are conveniently viewed as frequency curves, in which the calculated standing wave frequency ω is plotted against initial crest acceleration A_c for a given depth. For a spatial discretization $N = 64$, Fig. 1 gives a series of computed frequency curves alongside the corresponding results from Ref. 15, revealing considerable discrepancies. At each depth the computed frequencies from Ref. 15 are lower than those given here and the discrepancy increases with A_c, while the overall disagreement becomes more pronounced at smaller depths. This is due to a neglect of the zero mean height condition (6) in Ref. 15, and serves to illustrate the numerical importance of this condition, particularly at smaller depths. The results in Ref. 15 were validated against those of Vanden-Broeck and Schwartz[8] for the single depth of $d = 3.0$, almost half a wavelength, which is considered large in a hydrodynamics context. At this depth the discrepancy should be small across a wide portion of the A_c range, according to the observed behavior in Fig. 1. In addition, the arclength continuation method used here permits a wide exploration of the parameter space, capturing some critical nonlinear phenomena not observed in Ref. 15.

The obvious outstanding feature of the plots in Fig. 1 occurs at depth $d = 0.562$, in which multiple solution branches with turning points appear, producing up to three standing wave solutions with given initial crest acceleration A_c. In the left branch of this plot, ω increases from the linear fundamental value $\omega_0 = \sqrt{\tanh d}$ before the turn occurs, while the right branch turns twice, with a considerable gap between the branches where solutions were not found. This behavior is not isolated, and is closely associated with the phenomenon of harmonic resonance. A study of neighboring depths will now provide more insight into the nature of this connection.

Additional frequency curves for selected depths in the neighborhood of $d = 0.562$, scaled by their respective linear fundamental values ω_0, are given in Fig. 2, illustrating a persistent pair of opposing turning points from the left and right branches. As depth increases in the given range, the gap between the turning points passes through a local maximum before shrinking toward zero, while the entire structure shifts toward the ω axis. Figure 3 summarizes this behavior by
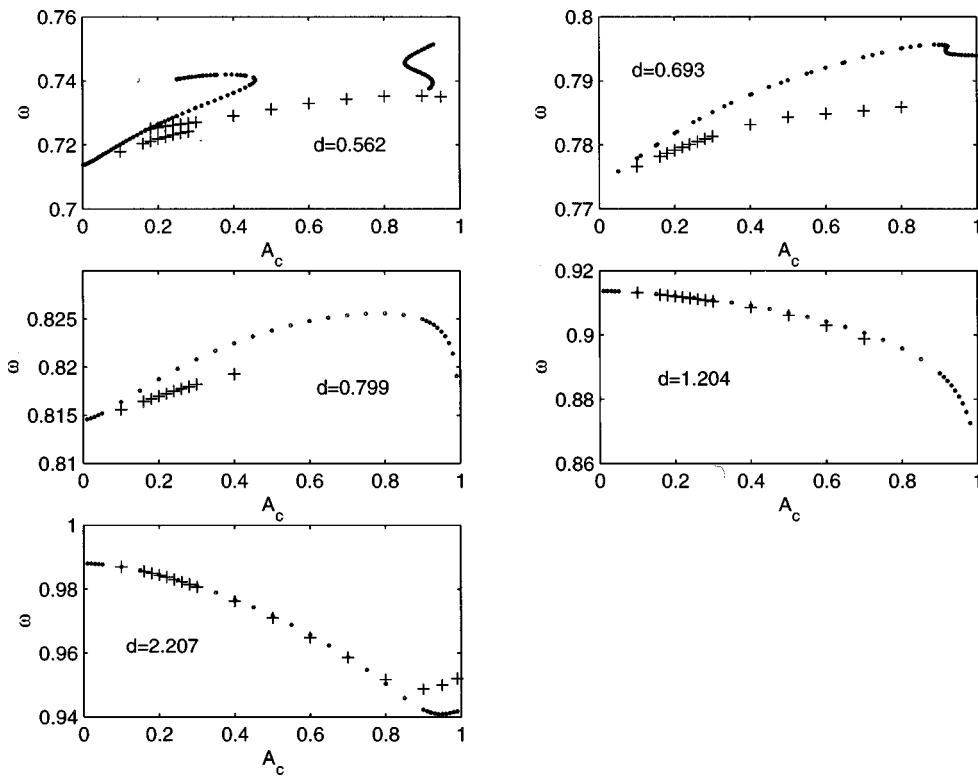
FIG. 1. A comparison of computed frequencies (dotted) with those in Ref. 15 (+), which did not enforce the zero mean height condition, for selected depths. The discrepancy between the two results increases with A_c at a given depth, with the overall disagreement diminishing as depth increases. At the relatively large depth $d = 2.207$ the discrepancy persists only for $A_c > 0.8$.

plotting the location of both (left and right) turning points against depth, revealing the shape of a corresponding ''hole'' in the (d, A_c, ω) solution surface. The ''beginning'' of this hole marks the birth of the resonance in the linear regime ($A_c \rightarrow 0$) and coincides with a critical depth at which the turning points coalesce on the ω axis. Analytic predictions of

these resonant depths, at which nonuniqueness should occur, are available from the formula[9]

$$\sqrt{n \tanh nd} = m \sqrt{\tanh d}, \quad m = 1, 2, \ldots, \quad n = 2, 3, \ldots, \quad (15)$$

which states that the frequency of the nth spatial harmonic is
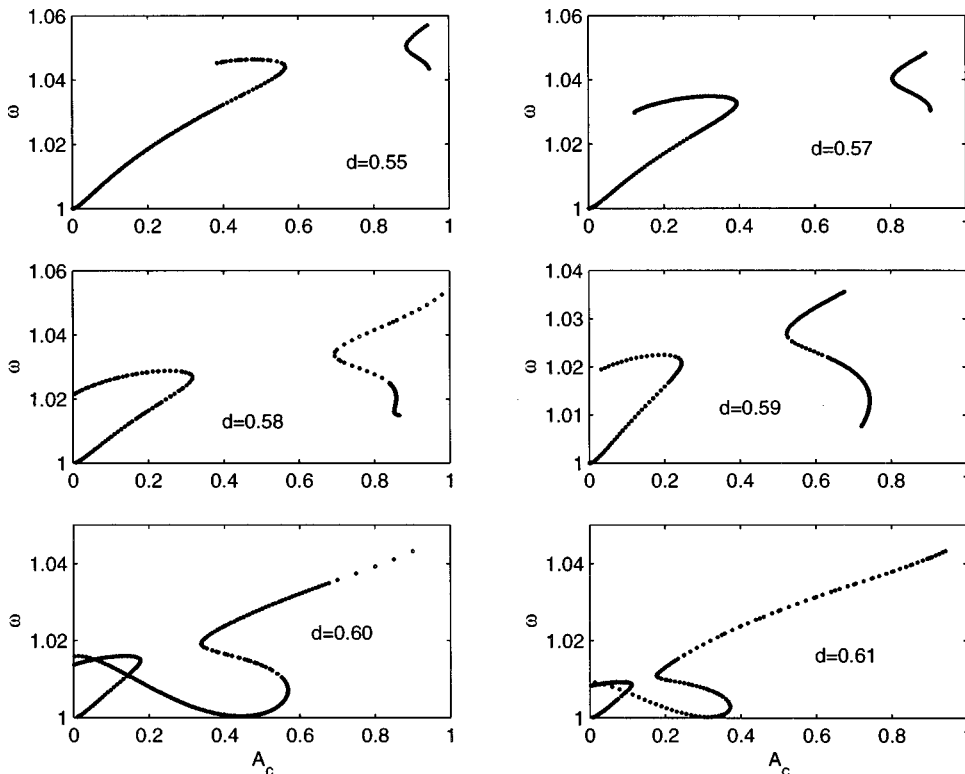
FIG. 2. The computed frequency curves for selected depths in the neighborhood of $d = 0.562$, illustrating the persistence of a pair of opposing turning points from the left and right branches. (Frequencies are scaled with respect to the linear fundamental value $\omega_0 = \sqrt{\tanh d}$.)
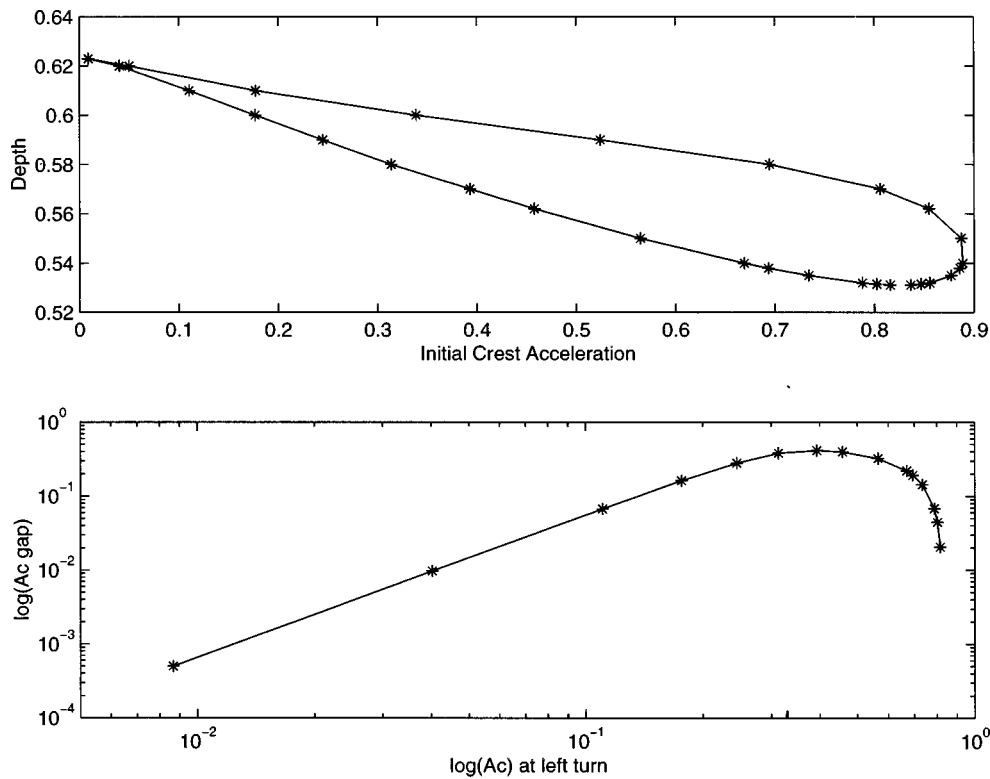
FIG. 3. The upper plot gives computed locations of the left and right turning points in a depth range bounded above by the (3,5) resonant depth. This view looks down on the (d, A_c, ω) solution surface, revealing the resonance "hole." The lower plot indicates the strength of the resonance, in terms of gap size between the turning point pairs, and its dependence on A_c, as measured at the left turn. A linear portion confirms near second order dependence for A_c < 0.3.

an integral multiple, m, of the fundamental frequency. In this case the appropriate resonant depth is d = 0.623 235 426 80... for $(m,n) = (3,5)$, corresponding to a resonant interaction between the fundamental and fifth harmonic, with the frequency of the latter being three times that of the fundamental.

At the other end of the hole, $d \approx 0.53$, the turning points coalesce again, with further depth reductions yielding "upper" and "lower" branches in the frequency curves, as shown in Fig. 4. The plot progresses through several depths in this neighborhood, showing the turning points just before the hole closes and what appears as a pair of rotated turning points just after. Geometrically, this is clarified by returning to Fig. 3 and picturing the hole outline as a rim over which the solution surface folds. Sections normal to the page, parallel to the A_c axis, yield opposing turning point pairs in the hole, and upper/lower branch pairs below the hole, as seen for $d = 0.5311$ in Fig. 4. The actual size of the A_c gap between the turning points is in some sense a measure of the strength of the resonance, and this is plotted against crest acceleration (at the left turning point) in Fig. 3. A linear portion of the plot with approximate slope 1.9 indicates near-second-order behavior in this respect.

Concus[10] gave a modified version of the nonuniqueness condition (15) for standing capillary–gravity waves, and showed that the resulting critical depths produced zero denominators in the perturbation solution coefficients, resulting in so-called harmonic resonance. As a resonant depth is approached, small nonzero denominators produce large coeffi-

cients for particular harmonics, increasing their relative contribution to the overall solution. With regard to the previous results, it will be shown that the fifth harmonic indeed fits this category, however, it is interesting to note that the associated near-resonant behavior is only observed at depths below the predicted critical depth. Near-resonant behaviour can be studied analytically using detuning parameters,[16] a concept employed by Roberts[17] to explore the links between nonuniqueness and resonance in the perturbation study of a model wave equation. In this study up to three solutions were found near resonance points, supporting a general conclusion that resonance induces multiple solutions, as witnessed in Figures 1 and 2. Further work by Concus[12] showed that the set of resonant depths, satisfying (15), is densely distributed on $(0, \infty)$ and that for any fluid depth there are infinitely many resonant or near resonant terms in a perturbation expansion. High order terms of comparable magnitude to the low order terms must necessarily be omitted from the truncated series, casting doubt on the validity of the procedure. Due to its finite spatial resolution, the numerical scheme under consideration here would also be subject to a similar phenomenon.

B. The (3,5) resonance

An obvious link has already been established between the observed branching behavior and the (3,5) resonance. To confirm these integer parameters and further substantiate the connection requires a closer examination of the computed results. First, spectral plots of the surface profiles indicate a
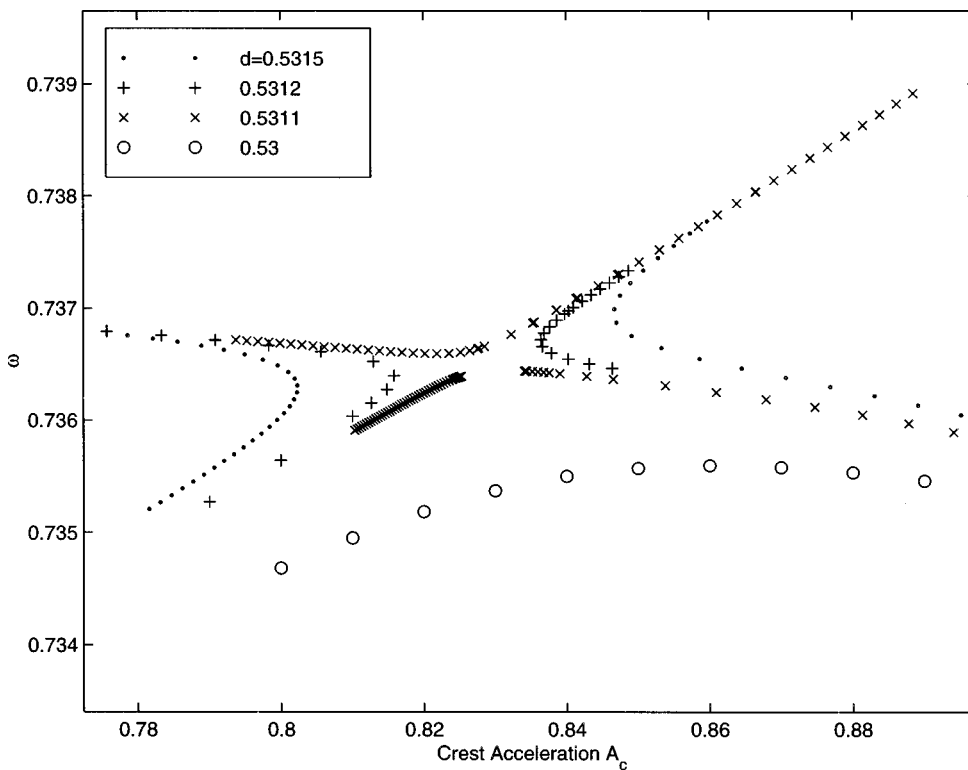
FIG. 4. Frequency curves for selected depths near the end of the hole outlined in Fig. 3. At $d=0.5315$ and 0.5312, before the hole ends, the familiar opposing turning points appear, while $d=0.5311$ and 0.53 produce upper/lower branch pairs. Only the lower branch is shown for $d=0.53$. At $d=0.5311$ ($\times$), convergence problems prevented a full tracing of the lower branch.

fifth harmonic presence in varying amounts along the branches of Fig. 2, from none to almost total dominance, reflecting the near-resonant character of the solutions. As a typical example consider the plot for $d=0.57$, from which representative surface profiles are given in Fig. 5, along with corresponding spatial spectra in Fig. 6. On the lower left and upper right branches the solutions are essentially pure fundamental, while those on the upper left and lower right branches are more oscillatory, due to the presence of the fifth harmonic, indicating the resonant interaction between these modes. Oscillation is considerably more pronounced in the upper left profile, which contains a sharp local maximum near the left wall and a broad local minimum near the right wall, features noticeably absent from the lower right profile. The turning points signify a transition between resonant and nonresonant solutions in each case, and contributions from the resonant harmonic increase along the resonant branch sections away from these points, giving more oscillatory profiles and amplifying the local maximum seen in Fig. 5.

Another important feature of the frequency curves in Fig. 2 is the local minimum appearing in the right-hand branch as the resonant depth is approached, for $d=0.60$ and 0.61. Graphically, the frequencies at these local minima appear to coincide with the linear fundamental frequency ω_0, while the corresponding surface profiles are almost purely fifth harmonic, as shown in Fig. 7 for $d=0.60$. However, time integration of these waves over the computed period shows that this value is not in fact the minimal wave period, but approximately three times this minimum, as the plot of $y(0,t)$ in Fig. 7 shows. Alternatively, the actual frequency is approximately three times the computed value, which is still perfectly computationally valid since a wave with period $T/3$

also has periods of $2T/3, T, \ldots$. A linear fundamental solution from the left-hand branch at small crest acceleration is also included in Fig. 7 to illustrate the frequency relationship between the two solutions.

More precise confirmation of the resonant frequency multiple $m=3$ is achieved by using the local minimum frequency solutions from Fig. 2 to compute new solutions at one-third the original computed period, then branch tracing from these back to the ω axis. This reveals entire families of pure fifth harmonics, with the frequency ratio ω/ω_0 converging to the value 3 on the ω axis as the resonant depth is approached. Branch sections for depths $d=0.60$, 0.61, 0.62, and 0.623 are shown in Fig. 8 to demonstrate this convergence.

Moving a final step closer to the (3,5) resonant depth, Fig. 9 zooms in on the small A_c (linear) behavior at $d=0.623$, where the gap between the turning points is approximately 5×10^{-4} in the vicinity of $A_c=0.009$. This strongly suggests convergence to a transcritical bifurcation[18] in the linear limit as the predicted resonant depth is approached. It could be said that the resonance grows from this transcritical bifurcation, which ''unfolds'' with nonlinearity to give a pair of turning points that move in the (A_c, ω) plane with depth-dependent separation. The resonance remains active across a range of decreasing depths until the turning points coalesce again at the nonlinear end of the ''hole'' in Fig. 3, with $d \approx 0.531$.

C. Other resonances

Further reductions in depth see the emergence of a new family of turning point structures belonging to the (4,8) reso-
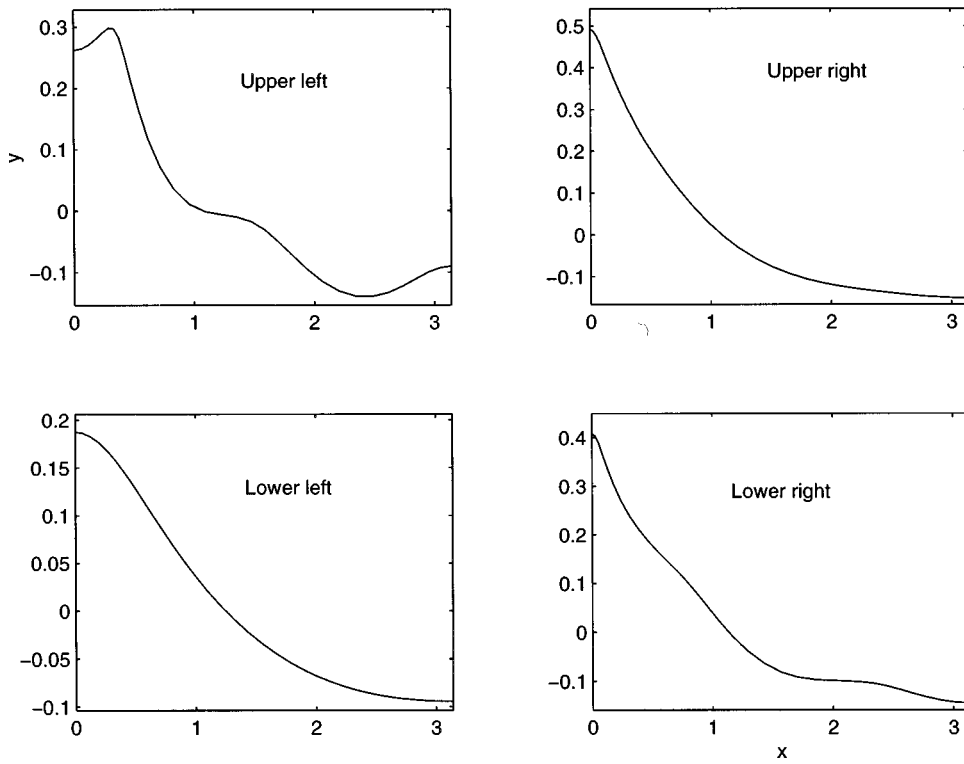
FIG. 5. Computed standing wave surface profiles from the upper left, upper right, lower left, and lower right branches for $d=0.57$ in Fig. 2. Resonant solutions containing a significant fifth harmonic component occur in the upper left and lower right branches.

nance, which has an associated critical depth d $=0.549\,102\,3...$. Figure 10 gives frequency curves for selected depths in this vicinity, indicating similar behavior to that observed for the (3,5) resonance. At $d=0.54$ the (3,5) resonance is still active, and nearing the end of its life, while the local minimum in the central branch is a pure eighth harmonic with frequency four times the linear fundamental value, as shown in Fig. 11.

The branching behavior of the (4,8) resonance is essentially a scaled replica of that from the (3,5) resonance, with smaller gaps between the turning points and a narrower active depth range, as illustrated in the comparison of Fig. 12. Corresponding solution profiles also exhibit similar behavior along the branches, with resonant solutions occupying the upper left and lower right segments. Sample (4,8) resonant solution profiles at $d=0.5$ are shown in Fig. 13, displaying
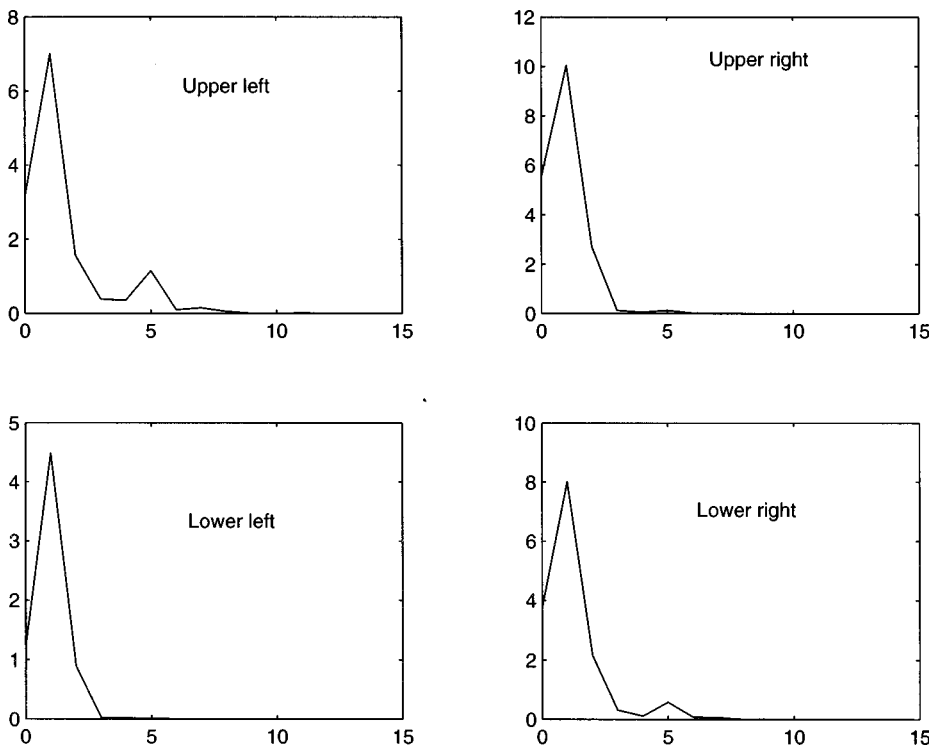
FIG. 6. Spectrum plots of the surface profiles given in Fig. 5, showing a fifth harmonic presence in the resonant solutions of the upper left and lower right branches.
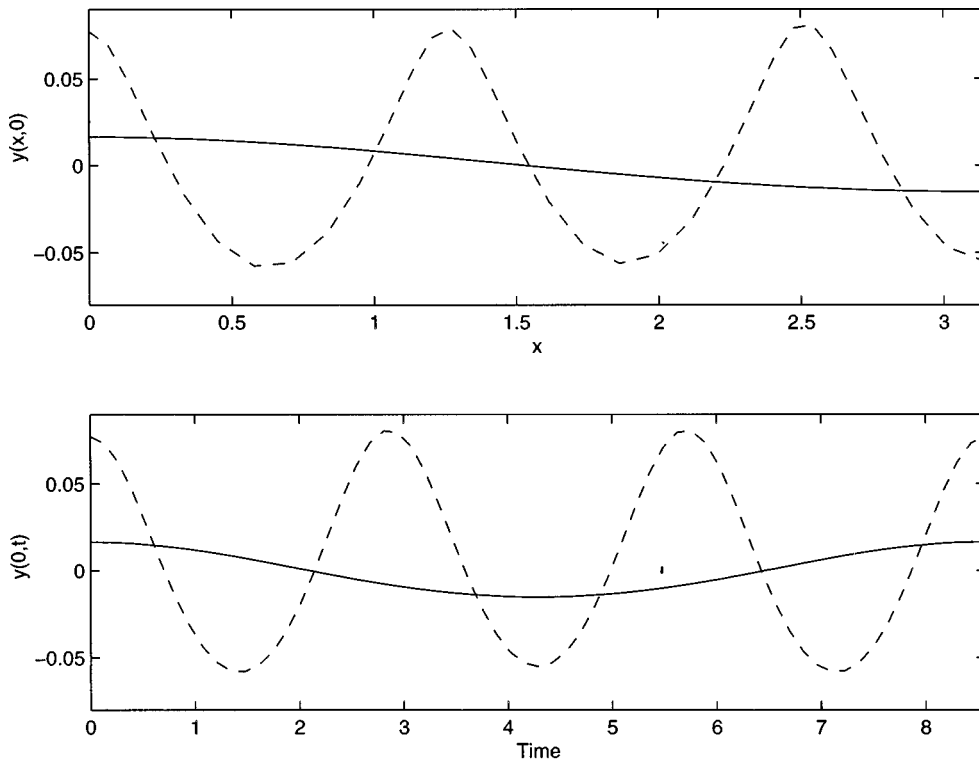
FIG. 7. Computed initial profile $y(x,0)$ and time history $y(0,t)$ for linear (solid line) and near fifth harmonic (dashed line) solutions at $d=0.60$. The time history plot indicates a frequency ratio of approximately 3, representing behavior near the (3,5) resonance.

more oscillatory behavior away from the turning points due to the growth of the eighth harmonic contribution. Proportionally, this contribution is noticeably smaller than the fifth harmonic contributions to the (3,5) resonant solutions, confirming relative weakness of the (4,8) resonance. Local maxima are also present near the left wall for upper left branch solutions, as seen in the (3,5) resonance, and a log plot of the turning point gap dependence confirms preservation of near-second-order behavior in A_c.

Turning point structures produced by the (3,5) and (4,8) resonances represent one of two possible unfolding configurations for transcritical bifurcations.[18] The question now
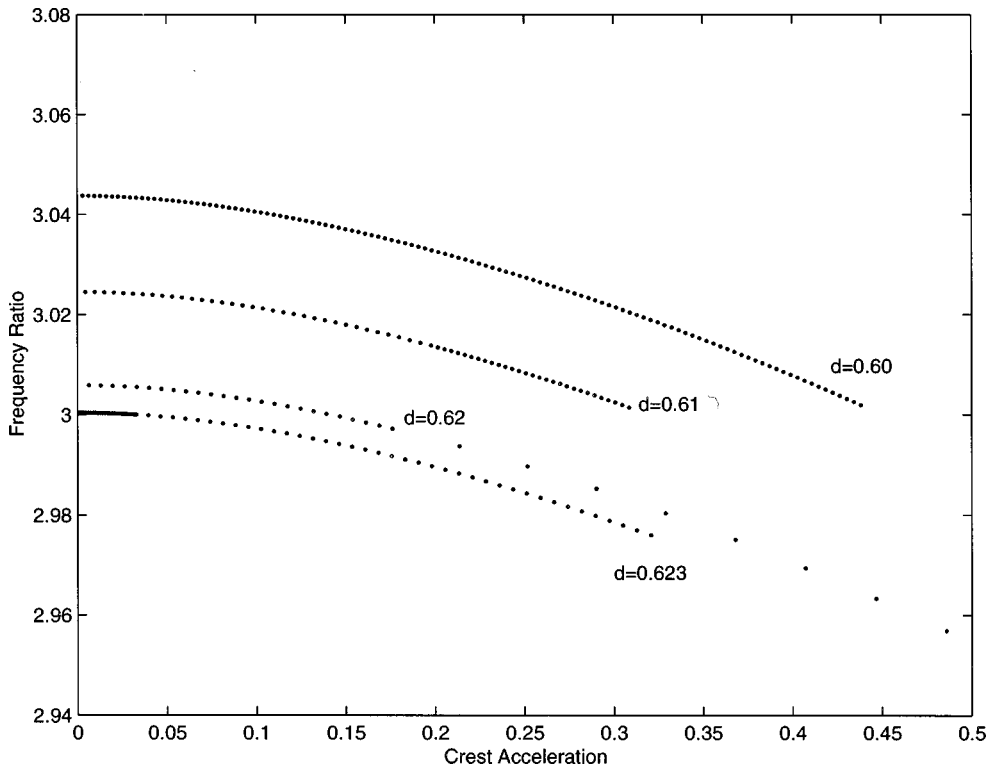
FIG. 8. Computed pure fifth harmonic branch sections, showing convergence to the frequency ratio $m=3$ for linear waves $(A_c \to 0)$ as the (3,5) resonant depth is approached. These curves are derived from the local minima in Fig. 2, where the computed standing wave periods are approximately three times the minimal period, and the spatial structure is nearly pure fifth harmonic.
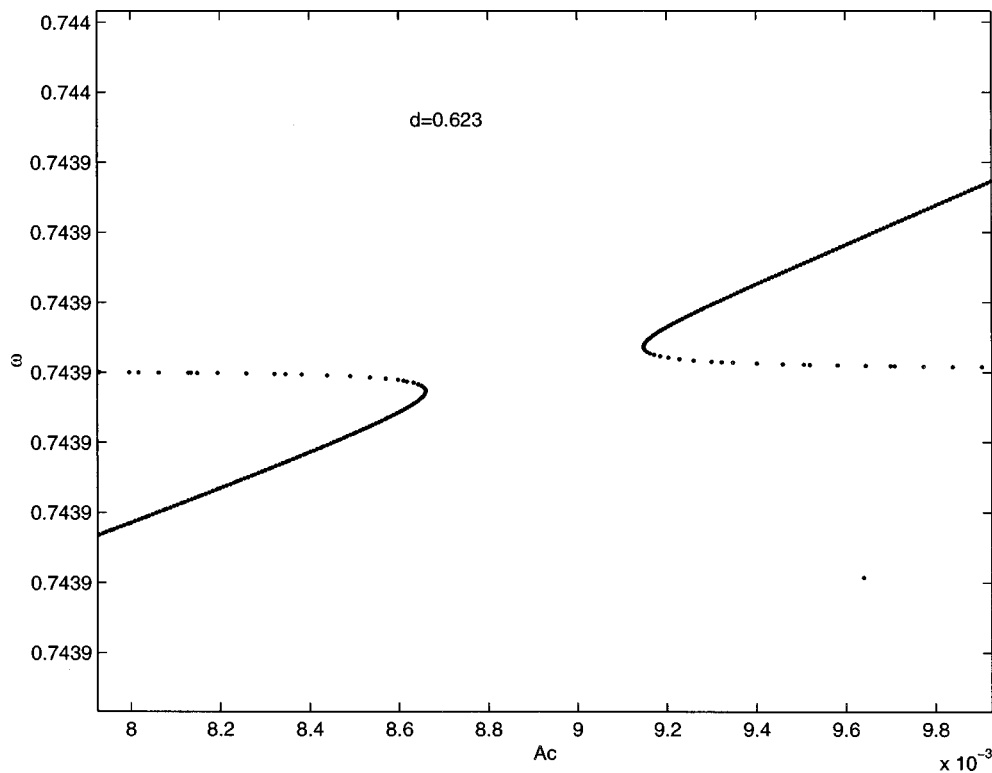
FIG. 9. The computed frequency curve for $d = 0.623$, showing the approach to a transcritical bifurcation in the linear regime, $A_c \rightarrow 0$, as depth tends to the (3,5) resonant depth.

arises as to whether the alternative configuration, essentially a "rotated" turning point pair, can also occur in the frequency curves as a manifestation of resonance. In the remaining calculations some additional resonances at smaller depths will be considered, displaying a second resonant branching structure, which clearly coincides with this description.

Figure 14 gives a series of frequency branch sections at depths approaching the predicted (4,6) resonant depth $d = 0.3858...$. In each plot, upper and lower branches emanate from the ω axis and converge toward each other, reaching a minimum separation before diverging. The resulting structure is a "rotated" turning point pair which persists with a shrinking separation gap as the depth becomes critical, finally approaching a transcritical bifurcation in the linear regime. In terms of sixth harmonic contributions to the solution profiles, the turning points signify an exchange. As A_c increases the upper branch progressively loses its sixth harmonic component, becoming pure fundamental after the turn, while the lower branch is initially pure fundamental before turning to gain a sixth harmonic component. This varies in size along the branch, and $d = 0.38$ includes the familiar loop structure with local minumum of an almost pure sixth harmonic at four times the linear fundamental frequency. Apart from the orientation of the turning points, the behavior observed here is similar to that for the previous resonances, originating from a collision between fundamental and sixth harmonic solution branches.

Reducing the depth to 0.36 shifts, the (4,6) resonant structure to the right and enlarges the approach gap between the branches, while an additional similar structure emerges to

mark the (5,9) resonance, with predicted critical depth $d = 0.3759...$. As shown in Fig. 15, there are three branches present with fundamental, sixth harmonic, and ninth harmonic contributions. The lower branch starts on the ω axis with pure fundamental solutions before breaking right to give resonant ninth harmonic solutions, including a pure ninth harmonic at the local minimum with frequency five times the linear fundamental. A central branch contains resonant ninth harmonic solutions at the left and sixth harmonics on the right, separated by a fundamental section in the deflection vicinity. The upper branch starts with sixth harmonic resonant solutions before steepening to become pure fundamental, as for $d = 0.38$. Surface profiles at various locations on these branches are shown in Fig. 16, displaying sixth and ninth harmonic contributions. The familiar local maximum near the left wall is still present in solutions of the left branches.

This complicated triad of branches with simultaneous (4,6) and (5,9) resonant activity is unlike anything observed for the (3,5) and (4,8) resonances. Possible reasons for this include the larger critical depths for the latter resonances and the larger difference between these critical values.

IV. SUMMARY AND CONCLUSIONS

A numerical parameter study has revealed characteristic signatures of harmonic resonance in the frequency-crest acceleration branching diagrams for finite-depth standing gravity waves. Four different resonances have been recorded, with each producing a local frequency minimum of an almost pure nth harmonic at m times the linear fundamental
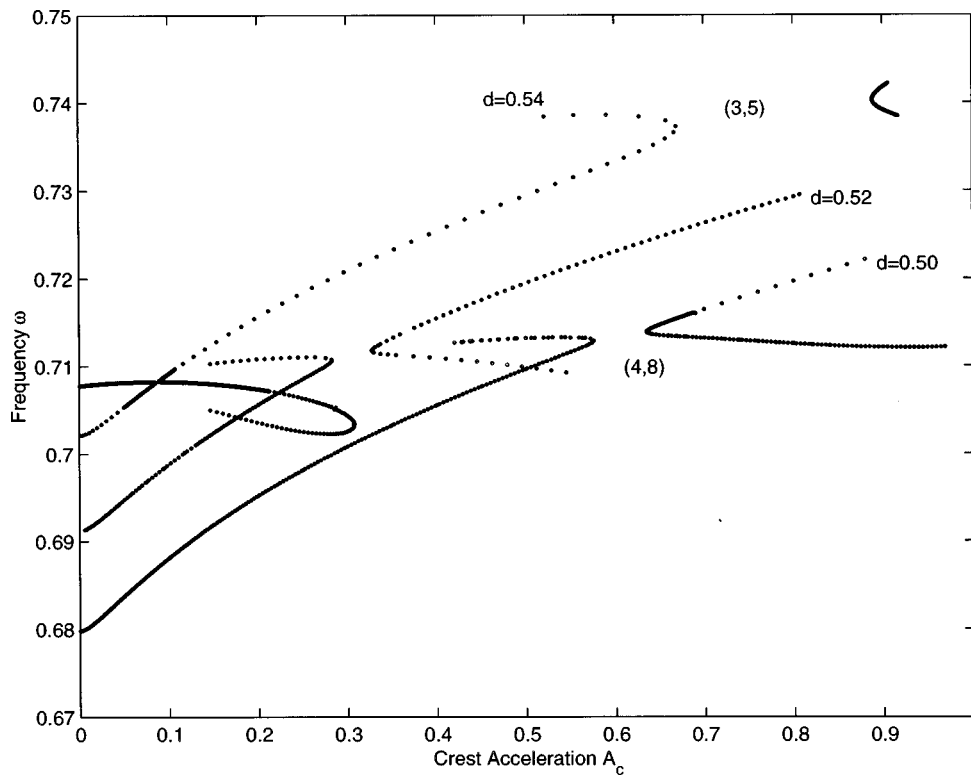
FIG. 10. Computed frequency curves at selected depths in the neighborhood of the (4,8) resonant depth, d $= 0.549\ 102\ 3...$. Similar behavior to that observed for the (3,5) resonance occurs, although on a smaller scale. Note that both resonances are active at $d = 0.54$.

frequency near the predicted (m,n) resonant depth. The most prominent observed signature was generated by the (3,5) resonance, which produced a persistent pair of turning points in the (A_c,ω) plane throughout a depth interval bounded above by the predicted (3,5) resonant depth. As this depth is approached from below, numerical evidence strongly suggests the formation of a transcritical bifurcation for linear waves, with a sufficiently small crest acceleration. Separation gaps between the turning points depend on depth, as does the actual location of the turning point pair in the
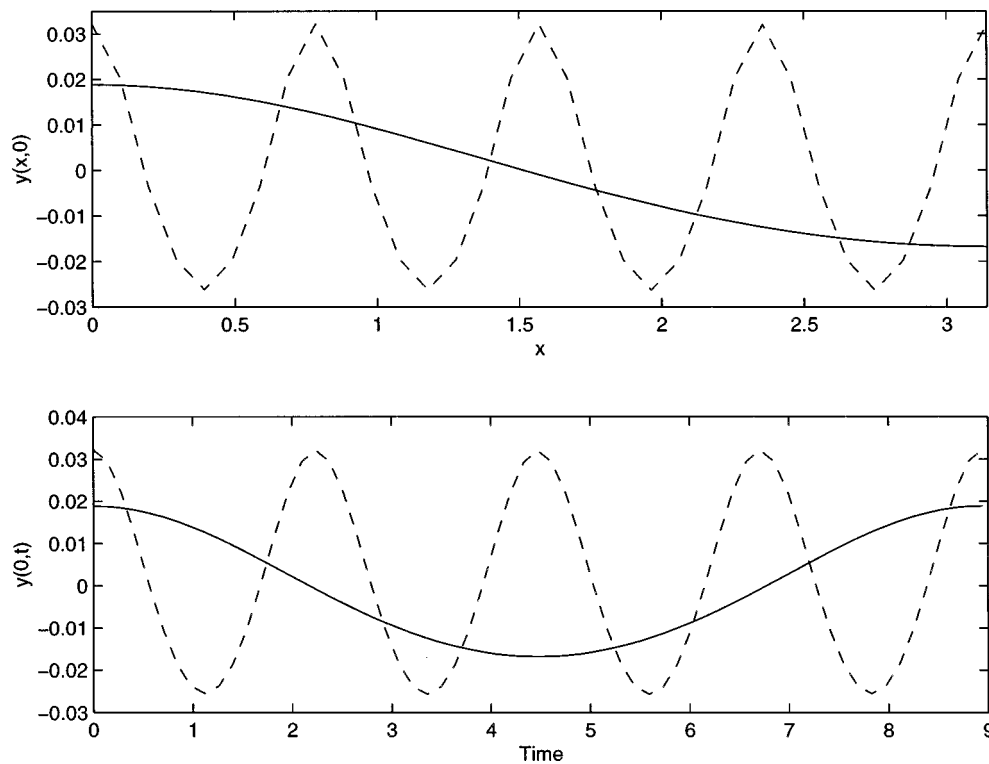

FIG. 11. Computed initial profiles, $y(x,0)$, and time history, $y(0,t)$, for linear fundamental ($A_c \approx 0.01$) and pure eighth harmonic solutions at $d = 0.54$. The pure eighth harmonic coincides with the local minimum frequency in the central branch for $d = 0.54$, Fig. 10.
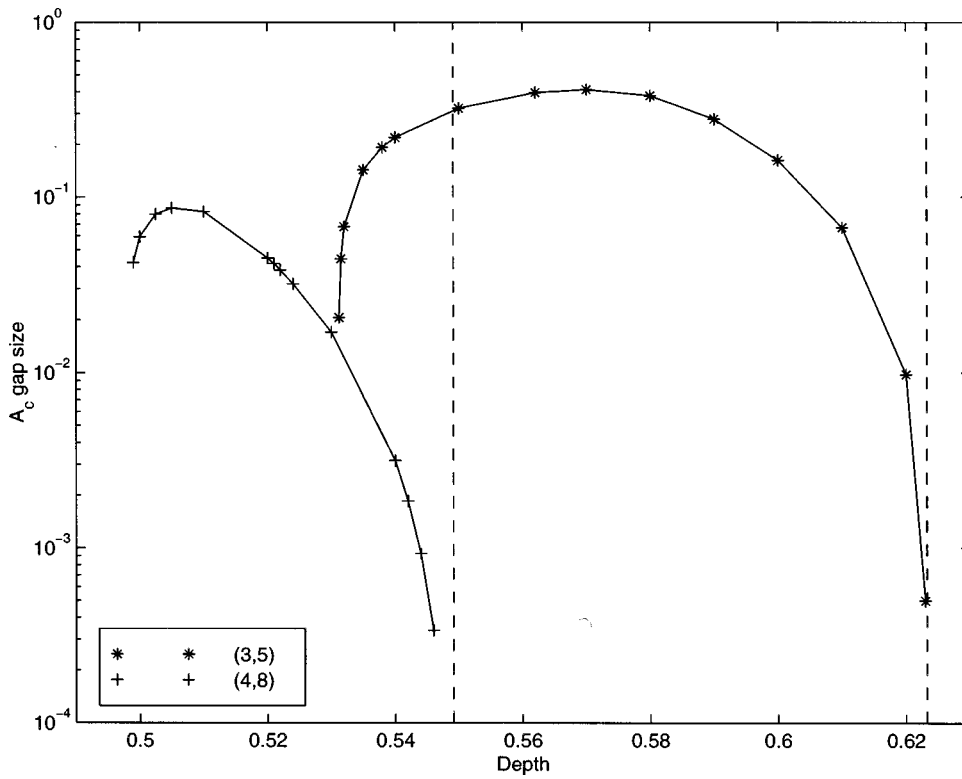
FIG. 12. The turning point gap size behavior for the (3,5) and (4,8) resonances, showing a larger active depth range for the (3,5) resonance, along with bigger gap sizes. The dashed lines indicate predicted resonant depths in each case, where the turning points appear to merge into a transcritical bifurcation in the linear regime.

(A_c, ω) plane. The overall effect of the resonance is to produce a ''hole'' in the (d, A_c, ω) solution surface, whose width achieves a maximum value at some point in the resonant depth interval.

The turning point behavior of the (3,5) resonance is essentially duplicated on a smaller scale for the (4,8) resonance, with smaller turning point gaps and a smaller resonant depth range. These factors, along with smaller solution contributions from the eighth harmonic make the (4,8) resonance weaker than the (3,5) in several ways. However, an important observed property common to both resonances is the near second order dependence of the turning point gap width on crest acceleration. The other two resonances considered, the (4,6) and (5,9), produced a slightly different signature,
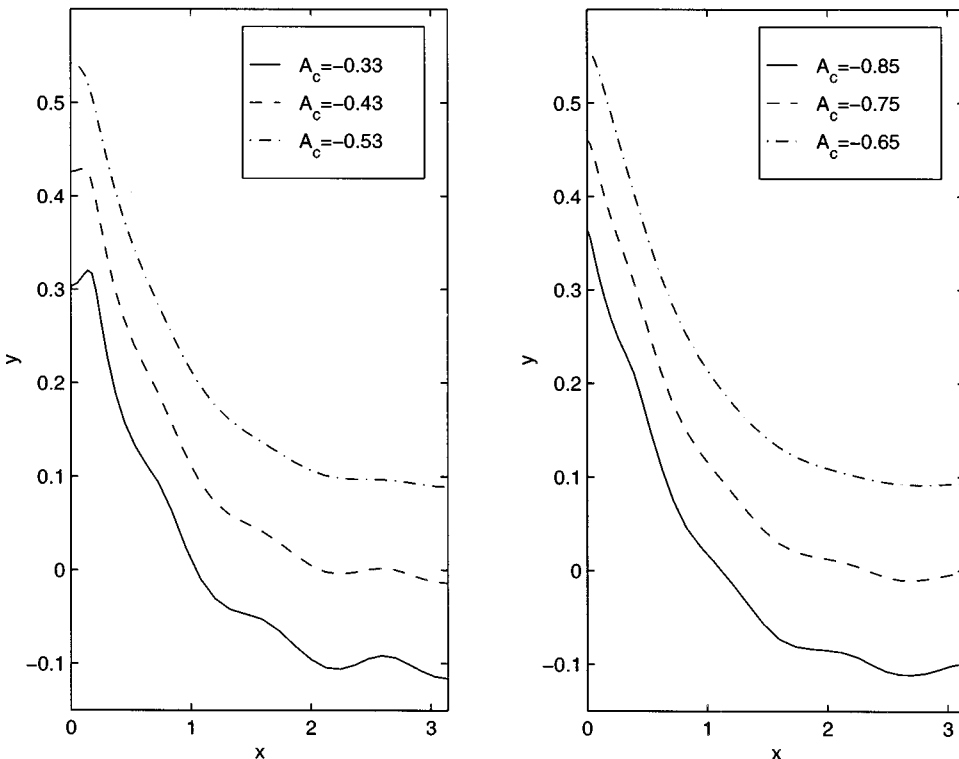

FIG. 13. Computed resonant solution profiles from the left and right branches of Fig. 10 at $d = 0.50$, with the mean level shifted for clarity. Relative contributions of the eighth harmonic increase away from the turning points to give more oscillatory profiles.
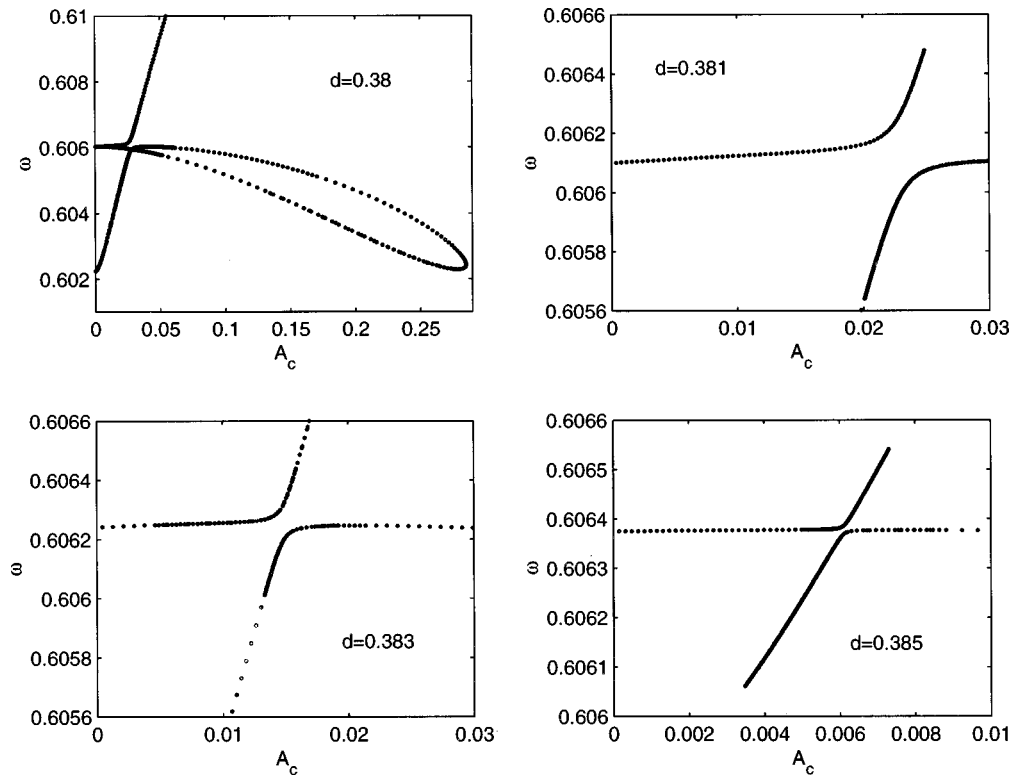
FIG. 14. A series of frequency curves at depths approaching the (4,6) resonant depth $d = 0.3858...$. Unlike the (3,5) and (4,8) resonant branching structures, the turning point pairs are now rotated, reflecting the alternative unfolding configuration for a transcritical bifurcation.

comprising ''rotated'' turning point pairs. These also move in the (A_c, ω) plane with variable separation and represent an alternative unfolding configuration for the branches of a transcritical bifurcation. Some complex branching patterns were observed for these resonances, whose critical depths are not only smaller but also considerably closer than those of the (3,5) and (4,8) resonances.

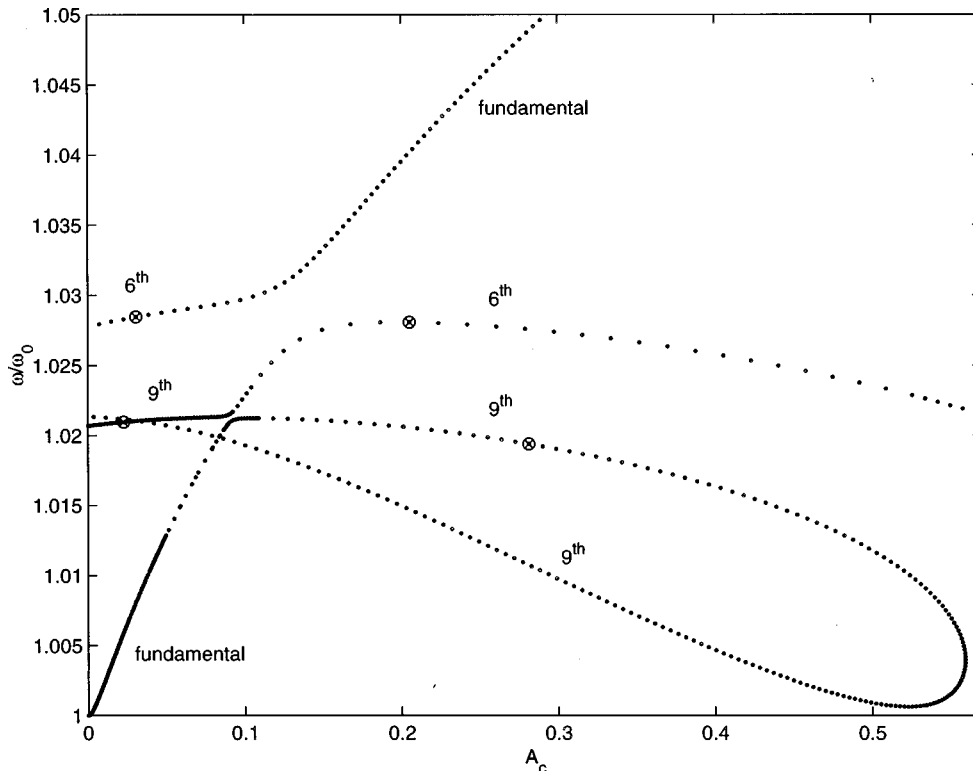In all four cases the turning point structures appeared to

FIG. 15. Computed frequency curves at $d = 0.36$, where the (4,6) and (5,9) resonances are simultaneously active. Frequencies have been scaled with respect to the linear fundamental value at this depth, and the local minimum in the lower branch is pure ninth harmonic at approximately five times the fundamental value. Surface profiles at the marked points are given in the plots of Fig. 16.
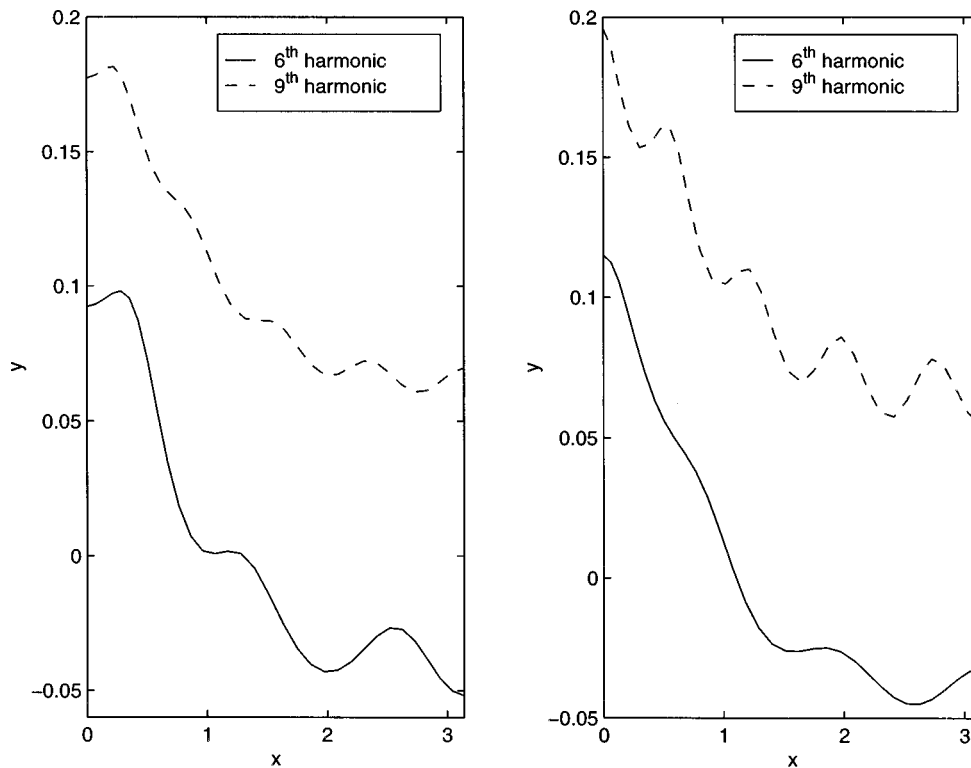
FIG. 16. Computed resonant solution profiles at $d = 0.36$, corresponding to the marked points on the branches of Fig. 15. The mean level has been shifted for clarity.

grow from a transcritical bifurcation in the linear regime at a predicted resonant depth. Nonlinearity corrupts the bifurcation to produce turning point pairs that ''move'' in the (A_c, ω) plane as depth varies in an interval bounded above by the predicted critical value.

ACKNOWLEDGMENTS

[1] O. M. Phillips, ''On the dynamics of unsteady gravity waves of finite amplitude, Part 1. The elementary interactions,'' J. Fluid Mech. **9**, 193 (1960).

[2] A. H. Nayfeh, ''Finite amplitude surface waves on a liquid layer,'' J. Fluid Mech. **40**, 671 (1970).

[3] B. Chen and P. G. Saffman, ''Steady gravity–capillary waves on deep water—I. Weakly nonlinear waves,'' Stud. Appl. Math. **60**, 183 (1979).

[4] M. Jones and J. Toland, ''Symmetry and the bifurcation of capillary–gravity waves,'' Arch. Ration. Mech. Anal. **96**, 29 (1986).

[5] H. Okamoto and M. Shoji, ''The resonance of modes in the problem of two-dimensional capillary–gravity waves,'' Physica D **95**, 336 (1996).

[6] P. J. Aston, ''Understanding the global solutions of the capillary–gravity wave problem,'' Wave Motion **17**, 113 (1993).

[7] B. Chen and P. G. Saffman, ''Numerical evidence for the existence of new types of gravity waves of permanent form on deep water,'' Stud. Appl. Math. **62**, 1 (1980).

[8] J. Vanden-Broeck and L. W. Schwartz, ''Numerical calculation of standing waves in water of arbitrary uniform depth,'' Phys. Fluids **24**, 812 (1981).

[9] I. Tadjbakhsh and J. B. Keller, ''Standing surface waves of finite amplitude,'' J. Fluid Mech. **8**, 442 (1960).

[10] P. Concus, ''Standing capillary–gravity waves of finite amplitude,'' J. Fluid Mech. **14**, 568 (1962).

[11] J-M. Vanden-Broeck, ''Nonlinear gravity–capillary standing waves in water of arbitrary uniform depth,'' J. Fluid Mech. **139**, 97 (1984).

[12] P. Concus, ''Standing capillary–gravity waves of finite amplitude: Corrigendum,'' J. Fluid Mech. **19**, 264 (1964).

[13] H. B. Keller, ''Numerical solution of bifurcation and nonlinear eigenvalue problems,'' in *Applications of Bifurcation Theory*, edited by P. H. Rabinowitz (Academic, New York, 1977).

[14] A. J. Roberts, ''A stable and accurate numerical method to calculate the motion of a sharp interface between fluids,'' IMA J. Appl. Math. **31**, 13 (1983).

[15] G. N. Mercer and A. J. Roberts, ''The form of standing waves on finite depth water,'' Wave Motion **19**, 233 (1994).

[16] A. H. Nayfeh, *Introduction to Perturbation Techniques* (Wiley-Interscience, New York, 1993).

[17] A. J. Roberts, ''The behaviour of harmonic resonant steady solutions to a model differential equation,'' Q. J. Mech. Appl. Math. **34**, 287 (1981).

[18] R. Seydel, *From Equilibrium To Chaos* (Elsevier, New York, 1988).